

A Separable and Asymptotic-Preserving Dynamical Low-Rank Method for the Vlasov–Poisson–Fokker–Planck System

Shiheng Zhang* and Jingwei Hu†

January 21, 2026

Abstract

We present a dynamical low-rank (DLR) method for the Vlasov–Poisson–Fokker–Planck (VPFP) system. Our main contributions are two-fold: (i) a conservative spatial discretization of the Fokker–Planck operator that factors into velocity-only and space-only components, enabling efficient low-rank projection, and (ii) a time discretization within the DLR framework that properly handles stiff collisions. We propose both first-order and second-order low-rank IMEX schemes. For the first-order scheme, we prove an asymptotic-preserving (AP) property when the field fluctuation is small. Numerical experiments demonstrate accuracy, robustness, and AP property at modest ranks.

Key words. Vlasov–Poisson–Fokker–Planck (VPFP), dynamical low-rank (DLR), projector-splitting, asymptotic-preserving (AP), IMEX time integration

AMS subject classifications. 35Q83, 35Q84, 65F30, 65M06, 65M12

1 Introduction

Kinetic equations provide a mesoscopic description of dilute particle systems by evolving the phase-space distribution under transport, field effects, and collisions. In this work, we consider the Vlasov–Poisson–Fokker–Planck (VPFP) system

$$\partial_t f(x, v, t) + v \cdot \nabla_x f(x, v, t) + \frac{1}{\varepsilon} E(x, t) \cdot \nabla_v f(x, v, t) = \frac{1}{\varepsilon} (\Delta_v f(x, v, t) + \nabla_v \cdot (v f(x, v, t))), \quad (1.1)$$

where $f(x, v, t)$ is the distribution function depending on time t , position $x \in \Omega_x \subset \mathbb{R}^{d_x}$, and velocity $v \in \mathbb{R}^{d_v}$. $E(x, t)$ is the electric field governed by the Poisson equation with potential $\phi(x, t)$:

$$E(x, t) = -\nabla_x \phi(x, t), \quad -\Delta_x \phi(x, t) = \rho(x, t) - \eta(x), \quad (1.2)$$

where $\rho(x, t) = \int_{\mathbb{R}^{d_v}} f \, dv$ is the charge density and $\eta(x)$ is a given background charge satisfying the global neutrality condition $\int_{\Omega_x} (\rho(x, 0) - \eta(x)) \, dx = 0$. The collision operator on the right-hand side of (1.1) is the classical linear Fokker–Planck operator [6, 19]. $\varepsilon > 0$ is a nondimensional parameter determining the strength

*Department of Applied Mathematics, University of Washington, Seattle, WA 98195 (shzhang3@uw.edu). Corresponding author.

†Department of Applied Mathematics, University of Washington, Seattle, WA 98195 (hujw@uw.edu).

of both the electric field and collisions. Since $E(x, t)$ is independent of v , we have $\nabla_v \cdot (Ef) = E \cdot \nabla_v f$. We may absorb the high-field drift into the right-hand side of (1.1) to obtain a more succinct form

$$\partial_t f + v \cdot \nabla_x f = \frac{1}{\varepsilon} \nabla_v \cdot \left(M \nabla_v \left(\frac{f}{M} \right) \right), \quad (1.3)$$

where the local Maxwellian M is defined as

$$M(x, v, t) = \frac{1}{(2\pi)^{d_v/2}} \exp \left(-\frac{1}{2} |v - E(x, t)|^2 \right). \quad (1.4)$$

The regime $\varepsilon \rightarrow 0$ is characterized by rapid relaxation in velocity and macroscopic high-field dynamics in physical space [16, 17, 18, 3]. Taking the zeroth and first velocity moments of (1.3) (i.e., $\int \cdot \, dv$ and $\int \cdot \cdot v \, dv$) yields the continuity and momentum balances

$$\partial_t \rho + \nabla_x \cdot J = 0, \quad (1.5)$$

$$\partial_t J + \nabla_x \cdot \int_{\mathbb{R}^{d_v}} v \otimes v f \, dv = \frac{1}{\varepsilon} (\rho E - J), \quad (1.6)$$

where $J(x, t) = \int f v \, dv$ is the current density. In the high-field limit, the stiff relaxation on the right-hand side of (1.6) drives $J \approx \rho E$ to leading order. Substituting this into (1.5) yields the closed macroscopic system

$$\begin{cases} \partial_t \rho + \nabla_x \cdot (\rho E) = 0, \\ E = -\nabla_x \phi, \quad -\Delta_x \phi = \rho - \eta. \end{cases} \quad (1.7)$$

This macroscopic drift system represents the high-field limit of the VPFP system as $\varepsilon \rightarrow 0$.

Numerical simulation of the VPFP system presents two principal difficulties: high dimensionality and stiffness. The phase-space distribution $f(x, v, t)$ evolves in $\mathbb{R}^{d_x + d_v}$. Discretizing this domain leads to computational and storage costs on the order of $\mathcal{O}(N_x^{d_x} N_v^{d_v})$, which becomes prohibitive in high dimensions. To mitigate this “curse of dimensionality”, a promising approach is the dynamical low-rank (DLR) approximation [13, 15]. This approach constrains the solution to a manifold of fixed rank r :

$$f(x, v, t) \approx \sum_{i,j=1}^r X_i(x, t) S_{ij}(t) V_j(v, t),$$

where the orthonormal factors $\{X_i\}_{i=1}^r$ and $\{V_j\}_{j=1}^r$ are evolved by projecting the governing equation onto the tangent space of the low-rank manifold. The efficiency of the DLR approximation relies critically on the structure of the operators in the governing equation. When the operator exhibits a separable structure in x and v , the computational cost scales as $\mathcal{O}(r^2(N_x^{d_x} + N_v^{d_v}) + r^4)$, and the storage requirement scales as $\mathcal{O}(r(N_x^{d_x} + N_v^{d_v}) + r^2)$. This substantial saving in the regime $r \ll \min\{N_x^{d_x}, N_v^{d_v}\}$ is what makes high-dimensional kinetic simulations feasible. In contrast, if the operator lacks a separable structure, evaluating the dynamics typically requires reconstructing the full tensor, which reverts the cost to the prohibitive $\mathcal{O}(N_x^{d_x} N_v^{d_v})$. Recently developed interpolatory DLR methods [1, 5] bypass this issue by employing collocation or empirical interpolation. However, additional error is introduced by replacing the orthogonal projection in the DLR method with an oblique projection. There are many other recent developments on DLR methods applied to general kinetic equations and we refer the reader to the review paper [7].

Due to the stiff field term and collision term, applying the DLR method to the VPFP system in the high-field regime is not straightforward. Explicit time integration requires restrictive time steps $\Delta t = \mathcal{O}(\varepsilon)$. This

necessitates asymptotic-preserving (AP) schemes, which allow ε -independent time steps while recovering the correct macroscopic limit [9, 10]. While AP schemes for the VPFP system are well-established for full-tensor methods [11, 2, 21], extending them to the DLR framework is non-trivial. The central difficulty lies in the Fokker–Planck operator on the right-hand side of (1.3): the spatially varying field $E(x, t)$ creates a strong coupling between x and v that destroys the separability required for efficient low-rank projection¹. This non-separability issue was addressed in [4] by evolving the quotient f/M rather than f , followed by a complicated change of variables. In this paper, we propose a direct approach: a conservative and separable discretization of the Fokker–Planck operator that allows efficient low-rank projection without variable transformation or full tensor reconstruction. Furthermore, the stiff Fokker–Planck operator in the low-rank framework requires careful time discretization to ensure stability. We propose both first-order and second-order low-rank IMEX schemes. For the first-order scheme, we prove an AP property when the field fluctuation is small.

The rest of this paper is organized as follows. Section 2 establishes the dynamical low-rank formulation for the VPFP system. Section 3 describes the separable, conservative discretization of the Fokker–Planck operator and its low-rank projection. Section 4 presents the fully discrete first-order and second-order low-rank IMEX schemes. Section 5 provides the asymptotic-preserving analysis for the first-order low-rank scheme. Section 6 reports numerical experiments demonstrating the accuracy and robustness of the proposed methods, and we conclude in Section 7.

2 Dynamical low-rank formulation for the VPFP system

In this section, we describe the projector-splitting dynamical low-rank (DLR) method, originally proposed by Lubich and Oseledets [15], applied to the VPFP system adopting the form (1.3). We define the advection operator \mathcal{A} and the Fokker–Planck operator \mathcal{L} as

$$\mathcal{A}(f) := -v \cdot \nabla_x f, \quad (2.1)$$

$$\mathcal{L}(f) := \nabla_v \cdot \left(M \nabla_v \left(\frac{f}{M} \right) \right), \quad (2.2)$$

so that (1.3) can be written as

$$\partial_t f = \mathcal{A}(f) + \frac{1}{\varepsilon} \mathcal{L}(f). \quad (2.3)$$

The DLR method approximates the solution $f(x, v, t)$ by constraining it to the manifold \mathcal{M}_r of rank- r functions. We employ the low-rank ansatz

$$f(x, v, t) = \sum_{i,j=1}^r X_i(x, t) S_{ij}(t) V_j(v, t), \quad (2.4)$$

where $S(t) \in \mathbb{R}^{r \times r}$ is the coefficient matrix, and $\{X_i(x, t)\}_{i=1}^r \subset L^2(\Omega_x)$ and $\{V_j(v, t)\}_{j=1}^r \subset L^2(\mathbb{R}^{d_v})$ are orthonormal bases satisfying

$$\langle X_i(\cdot, t), X_{i'}(\cdot, t) \rangle_x = \delta_{ii'}, \quad \langle V_j(\cdot, t), V_{j'}(\cdot, t) \rangle_v = \delta_{jj'}.$$

Here $\langle \phi, \psi \rangle_x := \int_{\Omega_x} \phi(x) \psi(x) dx$ and $\langle \phi, \psi \rangle_v := \int_{\mathbb{R}^{d_v}} \phi(v) \psi(v) dv$ denote the spatial and velocity inner products, respectively; we will also need $\langle \phi, \psi \rangle_{xv} := \int_{\Omega_x} \int_{\mathbb{R}^{d_v}} \phi(x, v) \psi(x, v) dx dv$ for the full phase-space inner product.

¹The separability is not an issue if one uses the original formulation (1.1). However, this form makes the design of an AP scheme difficult.

According to the Dirac–Frenkel variational principle [13, 14], the evolution of the low-rank approximation is determined by the orthogonal projection of the vector field $\mathcal{A}(f) + \frac{1}{\varepsilon}\mathcal{L}(f)$ onto the tangent space $T_f\mathcal{M}_r$ at the current approximation f :

$$\partial_t f = P_f(\mathcal{A}(f) + \frac{1}{\varepsilon}\mathcal{L}(f)). \quad (2.5)$$

The projection operator $P_f : L^2(\Omega_x \times \mathbb{R}^{d_v}) \rightarrow T_f\mathcal{M}_r$ is given explicitly by [15]:

$$P_f(g) = (I \otimes P_V)g - (P_X \otimes P_V)g + (P_X \otimes I)g, \quad (2.6)$$

where P_X and P_V are the orthogonal projectors onto the subspaces spanned by $\{X_i\}_{i=1}^r$ and $\{V_j\}_{j=1}^r$, respectively.

Direct integration of (2.5) is numerically challenging due to the curvature of the manifold. We employ the robust projector-splitting integrator [15], which splits the projection (2.6) into three coupled differential equations (K–S–L splitting) solved sequentially.

K-step (update the spatial basis). We first solve the subproblem corresponding to the term $(I \otimes P_V)(\mathcal{A} + \frac{1}{\varepsilon}\mathcal{L})(f)$. In this step, the velocity basis $\{V_j\}_{j=1}^r$ is frozen. We represent the solution as

$$f(x, v, t) = \sum_{j=1}^r K_j(x, t) V_j(v, t), \quad K_j(x, t) = \sum_{i=1}^r X_i(x, t) S_{ij}(t). \quad (2.7)$$

Projecting the dynamics onto the fixed basis V_j yields a system of r evolution equations for the spatial coefficients K_j :

$$\partial_t K_j(x, t) = \left\langle (\mathcal{A} + \frac{1}{\varepsilon}\mathcal{L}) \left(\sum_{\ell=1}^r K_\ell V_\ell \right), V_j \right\rangle_v, \quad j = 1, \dots, r. \quad (2.8)$$

After evolving (2.8) for one time step, a QR factorization of $\{K_j(\cdot, t^{n+1})\}_{j=1}^r$ yields the orthonormal spatial basis $\{X_i(x, t^{n+1})\}_{i=1}^r$ and an intermediate coefficient matrix $S^{(1)}$.

S-step (update the coefficient matrix). Next, we solve the subproblem corresponding to $-(P_X \otimes P_V)(\mathcal{A} + \frac{1}{\varepsilon}\mathcal{L})(f)$. Here, both bases are frozen. The evolution is restricted to the coefficient matrix S :

$$\frac{dS_{ij}}{dt} = - \left\langle (\mathcal{A} + \frac{1}{\varepsilon}\mathcal{L}) \left(\sum_{k, \ell=1}^r X_k S_{k\ell} V_\ell \right), X_i V_j \right\rangle_{xv}, \quad i, j = 1, \dots, r. \quad (2.9)$$

This step updates the coefficient matrix from $S^{(1)}$ to $S^{(2)}$. The negative sign implies this step effectively evolves backward in time.

L-step (update the velocity basis). Finally, we solve the subproblem corresponding to $(P_X \otimes I)(\mathcal{A} + \frac{1}{\varepsilon}\mathcal{L})(f)$. In this step, the spatial basis $\{X_i\}_{i=1}^r$ is frozen. We represent the solution as

$$f(x, v, t) = \sum_{i=1}^r X_i(x, t) L_i(v, t), \quad L_i(v, t) = \sum_{j=1}^r S_{ij}(t) V_j(v, t). \quad (2.10)$$

Projecting onto the fixed basis X_i yields r evolution equations for the velocity coefficients L_i :

$$\partial_t L_i(v, t) = \left\langle (\mathcal{A} + \frac{1}{\varepsilon}\mathcal{L}) \left(\sum_{k=1}^r X_k L_k \right), X_i \right\rangle_x, \quad i = 1, \dots, r. \quad (2.11)$$

After evolving (2.11) for one time step, a QR factorization of $\{L_i(\cdot, t^{n+1})\}_{i=1}^r$ yields the orthonormal velocity basis $\{V_j(v, t^{n+1})\}_{j=1}^r$ and the final coefficient matrix $S(t^{n+1})$.

Separability of the advection operator. The efficiency of the DLR method relies on the separability of the operator. The advection operator $\mathcal{A}(f) = -v \cdot \nabla_x f$ naturally satisfies this requirement. Its projection onto the low-rank basis does not require reconstructing the full distribution f . For example, in the K-step (2.8), the projection onto the velocity basis V_j becomes:

$$\langle \mathcal{A}(f), V_j \rangle_v = - \sum_{\ell=1}^r \langle v V_\ell, V_j \rangle_v \cdot \nabla_x K_\ell,$$

where the velocity and space dependent terms can be computed separately. If one chooses to discretize the differential operator first and then perform the projection, standard linear finite-difference approximations (e.g., upwind scheme) will preserve this separable structure.

The non-separable Fokker–Planck bottleneck. In contrast, the Fokker–Planck operator \mathcal{L} in (2.2) poses a significant challenge, where the Maxwellian function $M(x, v, t)$, as defined in (1.4), depends on the macroscopic electric field $E(x, t)$, introducing a non-trivial coupling between x and v . Consequently, its projection onto the low-rank basis, such as $\langle \mathcal{L}(f), X_i \rangle_x$, would generally require constructing the full tensor, incurring a computational cost of $\mathcal{O}(N_x^{d_x} N_v^{d_v})$, thereby defeating the purpose of the low-rank approach. Resolving this bottleneck is the primary contribution of this work: in Section 3, we propose a novel discrete formulation of \mathcal{L} that recovers a separable structure, enabling efficient DLR evolution.

3 Separable discretization of the Fokker–Planck operator and its low-rank projection

In this section, we construct a conservative finite-difference approximation of the Fokker–Planck operator (2.2) that decouples the spatial and velocity components. We then project this discrete operator onto the low-rank basis, demonstrating how this separable structure enables efficient DLR evolution.

We consider one spatial and one velocity dimension (1D1V) for simplicity; the approach can be extended to higher dimensions straightforwardly. We assume that the spatial and velocity domains are $[x_{\min}, x_{\max}]$ and $[v_{\min}, v_{\max}]$, respectively, with grid points given by

$$x_p = x_{\min} + \left(p - \frac{1}{2}\right) \Delta x, \quad p = 1, \dots, N_x, \quad v_q = v_{\min} + \left(q - \frac{1}{2}\right) \Delta v, \quad q = 1, \dots, N_v,$$

where $\Delta x = (x_{\max} - x_{\min})/N_x$ and $\Delta v = (v_{\max} - v_{\min})/N_v$. We impose periodic boundary condition in x and zero-flux boundary condition in v . The discrete low-rank ansatz for the distribution f at grid point (x_p, v_q) is

$$f_{p,q}(t) = \sum_{i=1}^r \sum_{j=1}^r X_{i,p}(t) S_{ij}(t) V_{j,q}(t), \quad (3.1)$$

where the basis vectors are orthonormal with respect to the discrete inner products defined by

$$\langle \phi, \psi \rangle_x^h = \sum_{p=1}^{N_x} \phi_p \psi_p \Delta x, \quad \langle \phi, \psi \rangle_v^h = \sum_{q=1}^{N_v} \phi_q \psi_q \Delta v.$$

The full phase-space inner product is given by

$$\langle \phi, \psi \rangle_{xv}^h = \sum_{p,q} \phi_{p,q} \psi_{p,q} \Delta x \Delta v.$$

3.1 Construction of the separable stencil

For the 1D1V Fokker–Planck operator $\mathcal{L}(f) = \partial_v(M\partial_v(f/M))$, we define its discretization at spatial grid point x_p and velocity grid point v_q as:

$$[\mathcal{L}_h(f)]_{p,q} = \frac{1}{\Delta v} \left(\mathcal{J}_{p,q+1/2} - \mathcal{J}_{p,q-1/2} \right), \quad (3.2)$$

where the flux $\mathcal{J}_{p,q+1/2}$ is given by

$$\mathcal{J}_{p,q+1/2} = M_{p,q+1/2} \frac{(f/M)_{p,q+1} - (f/M)_{p,q}}{\Delta v}, \quad M_{p,q+1/2} = \sqrt{M_{p,q} M_{p,q+1}}. \quad (3.3)$$

Note that we use a geometric-mean interpolation for the Maxwellian at the half grid point [12]. Other interpolations, such as the arithmetic mean $M_{p,q+1/2} = \frac{1}{2}(M_{p,q} + M_{p,q+1})$, are also possible, but would result in more terms in the separable expansion.

Substituting (3.3) into (3.2) yields the three-point conservative stencil:

$$[\mathcal{L}_h(f)]_{p,q} = \frac{1}{\Delta v^2} \left[\sqrt{\frac{M_{p,q}}{M_{p,q+1}}} f_{p,q+1} - \left(\sqrt{\frac{M_{p,q+1}}{M_{p,q}}} + \sqrt{\frac{M_{p,q-1}}{M_{p,q}}} \right) f_{p,q} + \sqrt{\frac{M_{p,q}}{M_{p,q-1}}} f_{p,q-1} \right]. \quad (3.4)$$

Using $v_{q+1} - v_q = \Delta v$ and $M_{p,q} \propto \exp(-(v_q - E_p)^2/2)$, we obtain

$$\sqrt{\frac{M_{p,q}}{M_{p,q+1}}} = \exp \left(\frac{(v_{q+1} - E_p)^2 - (v_q - E_p)^2}{4} \right) = \underbrace{\exp \left(\frac{\Delta v}{4} (v_q + v_{q+1}) \right)}_{:= \alpha_{q+1/2}} \underbrace{\exp \left(-\frac{\Delta v}{2} E_p \right)}_{:= \beta_p}. \quad (3.5)$$

Hence, it factors cleanly into space-only and velocity-only terms. Using the notation $\alpha_{q+1/2}$ and β_p , (3.4) can be written as

$$[\mathcal{L}_h(f)]_{p,q} = \frac{1}{\Delta v^2} \left[\alpha_{q+1/2} \beta_p f_{p,q+1} - \left(\frac{1}{\alpha_{q+1/2} \beta_p} + \alpha_{q-1/2} \beta_p \right) f_{p,q} + \frac{1}{\alpha_{q-1/2} \beta_p} f_{p,q-1} \right], \quad (3.6)$$

which is a fully separable stencil.

3.2 Low-rank projection

With the discretization (3.6), we now show that the projections onto the low-rank basis, as described in the previous section, can all be evaluated efficiently. For brevity, we focus only on the terms that involve the Fokker–Planck operator.

K-step. We compute the projection of the discrete operator $\mathcal{L}_h(f)$ onto the velocity basis V_j . Substituting the ansatz $f_{p,q} = \sum_{\ell=1}^r K_{\ell,p} V_{\ell,q}$ into (3.6), the p -th component of the projected term reads:

$$\begin{aligned} \left[\langle \mathcal{L}_h(f), V_j \rangle_v^h \right]_p &= \sum_{\ell=1}^r K_{\ell,p} \left[\frac{\beta_p}{\Delta v^2} \sum_{q=1}^{N_v} (\alpha_{q+1/2} V_{\ell,q+1} - \alpha_{q-1/2} V_{\ell,q}) V_{j,q} \Delta v \right. \\ &\quad \left. + \frac{1}{\beta_p \Delta v^2} \sum_{q=1}^{N_v} \left(\frac{V_{\ell,q-1}}{\alpha_{q-1/2}} - \frac{V_{\ell,q}}{\alpha_{q+1/2}} \right) V_{j,q} \Delta v \right]. \end{aligned} \quad (3.7)$$

S-step. We compute the projection of the discrete operator $\mathcal{L}_h(f)$ onto the tensor product basis $X_i V_j$. Substituting $f_{p,q} = \sum_{k,\ell} X_{k,p} S_{k\ell} V_{\ell,q}$ into (3.6), the double summation over space and velocity decouples:

$$\begin{aligned} \langle \mathcal{L}_h(f), X_i V_j \rangle_{xv}^h &= \sum_{k,\ell=1}^r S_{k\ell} \left[\left(\sum_{p=1}^{N_x} \beta_p X_{k,p} X_{i,p} \Delta x \right) \left(\frac{1}{\Delta v^2} \sum_{q=1}^{N_v} (\alpha_{q+1/2} V_{\ell,q+1} - \alpha_{q-1/2} V_{\ell,q}) V_{j,q} \Delta v \right) \right. \\ &\quad \left. + \left(\sum_{p=1}^{N_x} \frac{X_{k,p} X_{i,p}}{\beta_p} \Delta x \right) \left(\frac{1}{\Delta v^2} \sum_{q=1}^{N_v} \left(\frac{V_{\ell,q-1}}{\alpha_{q-1/2}} - \frac{V_{\ell,q}}{\alpha_{q+1/2}} \right) V_{j,q} \Delta v \right) \right]. \end{aligned} \quad (3.8)$$

L-step. We compute the projection of the discrete operator $\mathcal{L}_h(f)$ onto the spatial basis X_i . Substituting $f_{p,q} = \sum_{k=1}^r X_{k,p} L_{k,q}$ into (3.6), the q -th component of the projected term reads:

$$\begin{aligned} [\langle \mathcal{L}_h(f), X_i \rangle_x^h]_q &= \frac{1}{\Delta v^2} \sum_{k=1}^r \left[\left(\sum_{p=1}^{N_x} \beta_p X_{k,p} X_{i,p} \Delta x \right) (\alpha_{q+1/2} L_{k,q+1} - \alpha_{q-1/2} L_{k,q}) \right. \\ &\quad \left. + \left(\sum_{p=1}^{N_x} \frac{X_{k,p} X_{i,p}}{\beta_p} \Delta x \right) \left(\frac{L_{k,q-1}}{\alpha_{q-1/2}} - \frac{L_{k,q}}{\alpha_{q+1/2}} \right) \right]. \end{aligned} \quad (3.9)$$

4 Time discretization and the fully discrete low-rank scheme

Equation (2.3) involves an advection operator and a diffusive-type Fokker–Planck operator, the latter becoming stiff in the limit $\varepsilon \rightarrow 0$. A robust time integrator must handle this stiffness without imposing overly restrictive time steps, while preserving the correct asymptotic behavior. In the DLR setting, standard AP schemes cannot be applied straightforwardly; the projector-splitting structure, specifically the backward S-step, requires special stability considerations [20]. In this section, we propose first-order and second-order low-rank IMEX schemes. We employ the discretize-then-project strategy discussed in the previous section, but omit the subscripts p, q for simplicity.

4.1 A first-order scheme

We first present a simple first-order IMEX scheme in the full-tensor case, which serves as a basis for constructing the low-rank scheme. Let \mathcal{A}_h denote the discrete advection operator and $\mathcal{L}_h[E]$ denote the discrete Fokker–Planck operator constructed using the electric field E . A simple first-order IMEX scheme reads

$$\frac{f^{n+1} - f^n}{\Delta t} = \mathcal{A}_h(f^n) + \frac{1}{\varepsilon} \mathcal{L}_h[E^{n+1}](f^{n+1}). \quad (4.1)$$

Due to the dependence on E^{n+1} , directly solving for f^{n+1} would require iterations. To get around this, one can use the local mass conservation property, $\langle \mathcal{L}_h[E^{n+1}](f^{n+1}), 1 \rangle_v^h = 0$. Taking the zeroth moment of (4.1) yields

$$\frac{\rho^{n+1} - \rho^n}{\Delta t} = \langle \mathcal{A}_h(f^n), 1 \rangle_v^h, \quad \rho^n := \langle f^n, 1 \rangle_v^h. \quad (4.2)$$

Therefore, one can first compute ρ^{n+1} via (4.2), then solve the Poisson equation (1.2) to obtain E^{n+1} . With E^{n+1} known, the scheme (4.1) can be easily solved by inverting a linear operator.

4.1.1 A first-order low-rank IMEX scheme

In the low-rank framework, we first use (4.2) to obtain a prediction of the density, and then use this predicted density in the subsequent K-S-L steps to update the distribution function. Suppose that we start from the low-rank decomposition $f^n = \sum_{i,j=1}^r X_i^n S_{ij}^n V_j^n$. The predicted density is then computed as

$$\hat{\rho}^{n+1} = \rho^n + \Delta t \langle \mathcal{A}_h(f^n), 1 \rangle_v^h. \quad (4.3)$$

We distinguish the predicted density $\hat{\rho}^n$ from the true density ρ^n , defined through the moment of f^n , because the low-rank scheme introduced below does not strictly preserve mass. The Poisson equation is then solved using $\hat{\rho}^{n+1}$ to obtain E^{n+1} .

With the field E^{n+1} known, the Fokker–Planck operator becomes linear $\mathcal{L}_h^{n+1} := \mathcal{L}_h[E^{n+1}]$. We then apply the projector-splitting integrator to (2.3). However, applying the IMEX scheme (4.1) across all K-S-L steps leads to instability, because the S-step evolves backward in time. This behavior was first observed empirically in [4] and later proved in [20]. As suggested in [20], we propose a hybrid IMEX scheme: the K and L steps use an implicit (backward Euler) update for the Fokker–Planck operator, while the S step uses an explicit (forward Euler) update.

1. K-step. Define $K_j^n = \sum_{i=1}^r X_i^n S_{ij}^n$, and solve for $K_j^{(1)}$ using

$$\frac{K_j^{(1)} - K_j^n}{\Delta t} = \langle \mathcal{A}_h(f^n), V_j^n \rangle_v^h + \frac{1}{\varepsilon} \langle \mathcal{L}_h^{n+1}(f^{(1)}), V_j^n \rangle_v^h, \quad (4.4)$$

where $f^{(1)} = \sum_{j=1}^r K_j^{(1)} V_j^n$. Computing $\{K_j^{(1)}\}_{j=1}^r$ requires solving N_x decoupled $r \times r$ linear systems, one for each spatial grid point. A QR factorization of $\{K_j^{(1)}\}_{j=1}^r$ yields the new spatial basis $\{X_i^{n+1}\}_{i=1}^r$ and intermediate coefficient matrix $S^{(1)}$.

2. S-step. Solve for $S^{(2)}$ using

$$\frac{S_{ij}^{(2)} - S_{ij}^{(1)}}{\Delta t} = -\langle \mathcal{A}_h(f^{(1)}), X_i^{n+1} V_j^n \rangle_{xv}^h - \frac{1}{\varepsilon} \langle \mathcal{L}_h^{n+1}(f^{(1)}), X_i^{n+1} V_j^n \rangle_{xv}^h, \quad (4.5)$$

where $f^{(1)} = \sum_{i,j} X_i^{n+1} S_{ij}^{(1)} V_j^n$. Note that this is a fully explicit step.

3. L-step. Define $L_i^{(2)} = \sum_{j=1}^r S_{ij}^{(2)} V_j^n$, and solve for L_i^{n+1} using

$$\frac{L_i^{n+1} - L_i^{(2)}}{\Delta t} = \langle \mathcal{A}_h(f^{(2)}), X_i^{n+1} \rangle_x^h + \frac{1}{\varepsilon} \langle \mathcal{L}_h^{n+1}(f^{n+1}), X_i^{n+1} \rangle_x^h, \quad (4.6)$$

where $f^{(2)} = \sum_{i=1}^r X_i^{n+1} L_i^{(2)}$ and $f^{n+1} = \sum_{i=1}^r X_i^{n+1} L_i^{n+1}$. Computing $\{L_i^{n+1}\}_{i=1}^r$ requires solving a linear system of size $(rN_v) \times (rN_v)$, which is block-tridiagonal in the velocity grid with $r \times r$ blocks. A final QR factorization of $\{L_i^{n+1}\}_{i=1}^r$ yields the new velocity basis $\{V_j^{n+1}\}_{j=1}^r$ and coefficient matrix S^{n+1} .

4.2 A second-order scheme

To achieve higher temporal accuracy, we employ a particular second-order IMEX scheme used in [8]. This scheme is special in that its implicit tableau corresponds to the trapezoidal rule, which is required in the stability analysis established in [20] for applying DLR methods to stiff parabolic problems.

Algorithm 1 First-order low-rank IMEX scheme

Input: Rank- r factors $\{X_i^n\}_{i=1}^r, S^n, \{V_j^n\}_{j=1}^r$ at t^n .

Output: Rank- r factors $\{X_i^{n+1}\}_{i=1}^r, S^{n+1}, \{V_j^{n+1}\}_{j=1}^r$ at t^{n+1} .

Step 1: Density prediction

- 1: Compute density $\rho^n = \langle f^n, 1 \rangle_v^h$ and the predicted density $\hat{\rho}^{n+1} = \rho^n + \Delta t \langle \mathcal{A}_h(f^n), 1 \rangle_v^h$.
- 2: Solve the Poisson equation using $\hat{\rho}^{n+1}$ for E^{n+1} .
- 3: Define the Fokker–Planck operator $\mathcal{L}_h^{n+1} := \mathcal{L}_h[E^{n+1}]$.

Step 2: Lie–Trotter projector-splitting evolution

- 4: **K-step:** Update $\{K_j\}_{j=1}^r$ via Eq. (4.4).
 - 5: QR factorization yields $\{X_i^{n+1}\}_{i=1}^r$ and $S^{(1)}$.
 - 6: **S-step:** Update S from $S^{(1)}$ to $S^{(2)}$ via Eq. (4.5).
 - 7: **L-step:** Update $\{L_i\}_{i=1}^r$ via Eq. (4.6).
 - 8: QR factorization yields $\{V_j^{n+1}\}_{j=1}^r$ and S^{n+1} .
-

In the full-tensor case, the scheme reads

$$\frac{f^{n+1/2} - f^n}{\Delta t/2} = \mathcal{A}_h(f^n) + \frac{1}{\varepsilon} \mathcal{L}_h[E^{n+1/2}](f^{n+1/2}), \quad (4.7)$$

$$\frac{f^{n+1} - f^n}{\Delta t} = \mathcal{A}_h(f^{n+1/2}) + \frac{1}{2\varepsilon} \left(\mathcal{L}_h[E^n](f^n) + \mathcal{L}_h[E^{n+1}](f^{n+1}) \right). \quad (4.8)$$

To resolve the coupling with the unknown fields $E^{n+1/2}$ and E^{n+1} , similar strategy in the first-order scheme applies. Taking the zeroth moment of (4.7) yields

$$\rho^{n+1/2} = \rho^n + \frac{\Delta t}{2} \langle \mathcal{A}_h(f^n), 1 \rangle_v^h. \quad (4.9)$$

We solve the Poisson equation using $\rho^{n+1/2}$ to obtain $E^{n+1/2}$, allowing us to solve (4.7) efficiently for $f^{n+1/2}$. Similarly, taking the zeroth moment of (4.8) yields

$$\rho^{n+1} = \rho^n + \Delta t \langle \mathcal{A}_h(f^{n+1/2}), 1 \rangle_v^h. \quad (4.10)$$

With ρ^{n+1} (and thus E^{n+1}) determined, we finally solve (4.8) to obtain f^{n+1} .

4.2.1 A second-order low-rank IMEX scheme

In the low-rank framework, we first compute the predicted density at $t_{n+1/2}$:

$$\hat{\rho}^{n+1/2} = \rho^n + \frac{\Delta t}{2} \langle \mathcal{A}_h(f^n), 1 \rangle_v^h. \quad (4.11)$$

We then solve the Poisson equation using $\hat{\rho}^{n+1/2}$ to obtain $E^{n+1/2}$. To obtain E^{n+1} , we need $f^{n+1/2}$ which can be computed using the first-order low-rank scheme (Algorithm 1) with step size $\Delta t/2$. Then

$$\hat{\rho}^{n+1} = \rho^n + \Delta t \langle \mathcal{A}_h(f^{n+1/2}), 1 \rangle_v^h. \quad (4.12)$$

Solving the Poisson equation using $\hat{\rho}^{n+1}$ yields E^{n+1} . With the field $E^{n+1/2}$ and E^{n+1} known, the Fokker–Planck operator becomes $\mathcal{L}_h^{n+1/2} := \mathcal{L}_h[E^{n+1/2}]$ and $\mathcal{L}_h^{n+1} := \mathcal{L}_h[E^{n+1}]$.

We then apply the projector-splitting integrator to (2.3) using Strang splitting

$$\mathcal{K}(\frac{\Delta t}{2}) \circ \mathcal{S}(\frac{\Delta t}{2}) \circ \mathcal{L}(\Delta t) \circ \mathcal{S}(\frac{\Delta t}{2}) \circ \mathcal{K}(\frac{\Delta t}{2}).$$

In each substep, we employ the second-order IMEX scheme discussed above.

1. First K-step ($\Delta t/2$). Define $K_j^n = \sum_{i=1}^r X_i^n S_{ij}^n$, and solve for $K^{(1)}$ using

$$\frac{K_j^{n,*} - K_j^n}{\Delta t/4} = \langle \mathcal{A}_h(f[K^n]), V_j^n \rangle_v^h + \frac{1}{\varepsilon} \langle \mathcal{L}_h^{n+1/2}(f[K^{n,*}]), V_j^n \rangle_v^h, \quad (4.13)$$

$$\frac{K_j^{(1)} - K_j^n}{\Delta t/2} = \langle \mathcal{A}_h(f[K^{n,*}]), V_j^n \rangle_v^h + \frac{1}{2\varepsilon} \langle \mathcal{L}_h^n(f[K^n]) + \mathcal{L}_h^{n+1}(f[K^{(1)}]), V_j^n \rangle_v^h. \quad (4.14)$$

Here, $f[K] = \sum_{\ell} K_{\ell} V_{\ell}^n$. A QR factorization of $\{K_j^{(1)}\}_{j=1}^r$ yields the intermediate spatial basis $\{X_i^{(1)}\}_{i=1}^r$ and coefficient matrix $S^{(1)}$.

2. First S-step ($\Delta t/2$). Solve for $S^{(2)}$ using

$$\frac{S_{ij}^{(1)*} - S_{ij}^{(1)}}{\Delta t/4} = -\langle \mathcal{A}_h(f[S^{(1)}]), X_i^{(1)} V_j^n \rangle_{xv}^h - \frac{1}{\varepsilon} \langle \mathcal{L}_h^{n+1/2}(f[S^{(1)*}]), X_i^{(1)} V_j^n \rangle_{xv}^h, \quad (4.15)$$

$$\frac{S_{ij}^{(2)} - S_{ij}^{(1)}}{\Delta t/2} = -\langle \mathcal{A}_h(f[S^{(1)*}]), X_i^{(1)} V_j^n \rangle_{xv}^h - \frac{1}{2\varepsilon} \langle \mathcal{L}_h^n(f[S^{(1)}]) + \mathcal{L}_h^{n+1}(f[S^{(2)}]), X_i^{(1)} V_j^n \rangle_{xv}^h. \quad (4.16)$$

Here, $f[S] = \sum_{k,\ell} X_k^{(1)} S_{k\ell} V_{\ell}^n$.

3. L-step (Δt). Define $L_i^{(2)} = \sum_{j=1}^r S_{ij}^{(2)} V_j^n$, and solve for $L^{(3)}$ using

$$\frac{L_i^{(2)*} - L_i^{(2)}}{\Delta t/2} = \langle \mathcal{A}_h(f[L^{(2)}]), X_i^{(1)} V_j^n \rangle_x^h + \frac{1}{\varepsilon} \langle \mathcal{L}_h^{n+1/2}(f[L^{(2)*}]), X_i^{(1)} V_j^n \rangle_x^h, \quad (4.17)$$

$$\frac{L_i^{(3)} - L_i^{(2)}}{\Delta t} = \langle \mathcal{A}_h(f[L^{(2)*}]), X_i^{(1)} V_j^n \rangle_x^h + \frac{1}{2\varepsilon} \langle \mathcal{L}_h^n(f[L^{(2)}]) + \mathcal{L}_h^{n+1}(f[L^{(3)}]), X_i^{(1)} V_j^n \rangle_x^h. \quad (4.18)$$

Here, $f[L] = \sum_k X_k^{(1)} L_k$. A QR factorization of $\{L_i^{(3)}\}_{i=1}^r$ yields the new velocity basis $\{V_j^{n+1}\}_{j=1}^r$ and coefficient matrix $S^{(3)}$.

4. Second S-step ($\Delta t/2$). Solve for $S^{(4)}$ using

$$\frac{S_{ij}^{(3)*} - S_{ij}^{(3)}}{\Delta t/4} = -\langle \mathcal{A}_h(f[S^{(3)}]), X_i^{(1)} V_j^{n+1} \rangle_{xv}^h - \frac{1}{\varepsilon} \langle \mathcal{L}_h^{n+1/2}(f[S^{(3)*}]), X_i^{(1)} V_j^{n+1} \rangle_{xv}^h, \quad (4.19)$$

$$\frac{S_{ij}^{(4)} - S_{ij}^{(3)}}{\Delta t/2} = -\langle \mathcal{A}_h(f[S^{(3)*}]), X_i^{(1)} V_j^{n+1} \rangle_{xv}^h - \frac{1}{2\varepsilon} \langle \mathcal{L}_h^n(f[S^{(3)}]) + \mathcal{L}_h^{n+1}(f[S^{(4)}]), X_i^{(1)} V_j^{n+1} \rangle_{xv}^h. \quad (4.20)$$

Here, $f[S] = \sum_{k,\ell} X_k^{(1)} S_{k\ell} V_{\ell}^{n+1}$.

5. Second K-step ($\Delta t/2$). Define $K_j^{(4)} = \sum_{i=1}^r X_i^{(1)} S_{ij}^{(4)}$, and solve for K^{n+1} using

$$\frac{K_j^{(4)*} - K_j^{(4)}}{\Delta t/4} = \langle \mathcal{A}_h(f[K^{(4)}]), V_j^{n+1} \rangle_v^h + \frac{1}{\varepsilon} \langle \mathcal{L}_h^{n+1/2}(f[K^{(4)*}]), V_j^{n+1} \rangle_v^h, \quad (4.21)$$

$$\frac{K_j^{n+1} - K_j^{(4)}}{\Delta t/2} = \langle \mathcal{A}_h(f[K^{(4)*}]), V_j^{n+1} \rangle_v^h + \frac{1}{2\varepsilon} \langle \mathcal{L}_h^n(f[K^{(4)}]) + \mathcal{L}_h^{n+1}(f[K^{n+1}]), V_j^{n+1} \rangle_v^h. \quad (4.22)$$

Here, $f[K] = \sum_{\ell} K_{\ell} V_{\ell}^{n+1}$. A final QR factorization of $\{K_j^{n+1}\}_{j=1}^r$ yields the new spatial basis $\{X_i^{n+1}\}_{i=1}^r$ and coefficient matrix S^{n+1} .

Algorithm 2 Second-order low-rank IMEX scheme

Input: Rank- r factors $\{X_i^n\}_{i=1}^r, S^n, \{V_j^n\}_{j=1}^r$ at t^n .

Output: Rank- r factors $\{X_i^{n+1}\}_{i=1}^r, S^{n+1}, \{V_j^{n+1}\}_{j=1}^r$ at t^{n+1} .

Step 1: Density prediction

- 1: Compute density $\rho^n = \langle f^n, 1 \rangle_v^h$ and $\hat{\rho}^{n+1/2} = \rho^n + \frac{\Delta t}{2} \langle \mathcal{A}_h(f^n), 1 \rangle_v^h$.
- 2: Solve the Poisson equation using $\hat{\rho}^{n+1/2}$ for $E^{n+1/2}$.
- 3: Evolve $f^n \rightarrow f^{n+1/2}$ using Algorithm 1 for $\Delta t/2$ step.
- 4: Compute $\hat{\rho}^{n+1} = \rho^n + \Delta t \langle \mathcal{A}_h(f^{n+1/2}), 1 \rangle_v^h$.
- 5: Solve the Poisson equation using $\hat{\rho}^{n+1}$ for E^{n+1} .
- 6: Define $\mathcal{L}^n := \mathcal{L}[E^n], \mathcal{L}^{n+1/2} := \mathcal{L}[E^{n+1/2}], \mathcal{L}^{n+1} := \mathcal{L}[E^{n+1}]$.

Step 2: Strang projector-splitting evolution

- 7: **K-step** ($\Delta t/2$): Evolve $\{K_j\}_{j=1}^r$ via 2nd-order IMEX.
 - 8: QR factorization yields $\{X_i^{(1)}\}_{i=1}^r$ and $S^{(1)}$.
 - 9: **S-step** ($\Delta t/2$): Evolve S to obtain $S^{(2)}$ via 2nd-order IMEX.
 - 10: **L-step** (Δt): Evolve $\{L_i\}_{i=1}^r$ via 2nd-order IMEX.
 - 11: QR factorization yields $\{V_j^{n+1}\}_{j=1}^r$ and $S^{(3)}$.
 - 12: **S-step** ($\Delta t/2$): Evolve S to obtain $S^{(4)}$ via 2nd-order IMEX.
 - 13: **K-step** ($\Delta t/2$): Evolve $\{K_j\}_{j=1}^r$ via 2nd-order IMEX.
 - 14: QR factorization yields $\{X_i^{n+1}\}_{i=1}^r$ and S^{n+1} .
-

5 Asymptotic-preserving (AP) analysis

In this section, we analyze the asymptotic behavior of the proposed first-order low-rank IMEX scheme as $\varepsilon \rightarrow 0$. Our goal is to establish that the solution relaxes to the discrete Maxwellian determined by the macroscopic field, with a residual error controlled by ε and spatial field fluctuations.

We focus our analysis on the first-order scheme because it employs backward Euler time integration for the Fokker–Planck operator during the K and L steps. In the stiff limit, backward Euler is L -stable and acts as a projection onto the local equilibrium manifold, yielding a strongly AP scheme. This allows us to prove a global relaxation property via coercivity estimates.

5.1 Notation and micro-macro decomposition

We work in the 1D1V discrete setting and utilize the discrete norms and inner products defined in Section 3. Unless otherwise specified, operations involving the velocity inner product $\langle \cdot, \cdot \rangle_v^h$ are understood to map phase-space grid functions to spatial grid functions. Let $L_v = v_{\max} - v_{\min}$ denote the length of the velocity domain.

We assume without loss of generality that the discrete Maxwellian M is normalized on the velocity grid:

$$\langle M, 1 \rangle_v^h = 1. \quad (5.1)$$

Under this normalization, the local equilibrium is given by ρM , where the product implies row-wise scaling by the density vector.

To quantify the distance to equilibrium, we employ the standard micro-macro decomposition of the distribution function:

$$f = \rho M + g. \quad (5.2)$$

Here, ρM represents the projection of f onto the kernel of the Fokker–Planck operator (the local equilibrium manifold), and g represents the kinetic fluctuation. Due to the normalization of M and definition of the macroscopic density $\rho = \langle f, 1 \rangle_v^h$, the fluctuation satisfies the orthogonality property:

$$\langle g, 1 \rangle_v^h = 0. \quad (5.3)$$

Our goal is to bound the norm of the fluctuation:

$$\|f - \rho M\|_{xv}^h = \|g\|_{xv}^h. \quad (5.4)$$

For the analysis, we fix the field E^{n+1} and recall the space-dependent and velocity-dependent weights defined in (3.5):

$$\beta_p = \exp\left(-\frac{\Delta v}{2} E_p^{n+1}\right), \quad \alpha_{q+1/2} = \exp\left(\frac{\Delta v}{4} (v_q + v_{q+1})\right). \quad (5.5)$$

We assume we are in a regime where the spatial variation of the field is controlled. We denote the fluctuation of the spatial weights by $\delta\beta_p := \beta_p - \bar{\beta}$ relative to the spatial arithmetic mean $\bar{\beta}$, with $\|\delta\beta\|_\infty = \max_p |\beta_p - \bar{\beta}|$. This fluctuation serves as a proxy for the local rank of the Maxwellian; $\delta\beta \equiv 0$ corresponds to a spatially constant field where the Maxwellian is exactly separable (rank-1).

5.2 Key operator properties

We establish the key spectral properties of the discrete operator required for the main theorem. To obtain a coercive estimate for the Fokker–Planck operator, it is necessary to work with the relative fluctuation g/M .

Proposition 5.1 (Discrete coercivity). *Consider the decomposition $f = \rho M + g$, where the fluctuation satisfies the local mass conservation property $\langle g, 1 \rangle_v^h = 0$. There exists a constant $\gamma_h > 0$ such that the Fokker–Planck operator satisfies the coercivity estimate:*

$$-\langle \mathcal{L}_h(f), g/M \rangle_{xv}^h \geq \gamma_h \|g/M\|_{xv}^{h,2}, \quad (5.6)$$

where the constant γ_h is defined as:

$$\gamma_h := \frac{M_{\min} \lambda_N}{\left(1 + \sqrt{L_v M_{\max}}\right)^2}, \quad \text{with } \lambda_N = \frac{4}{\Delta v^2} \sin^2\left(\frac{\pi}{2N_v}\right). \quad (5.7)$$

Proof. Let $u = g/M$ denote the relative fluctuation grid function. Since $\mathcal{L}_{FP,h}(\rho M) = 0$, the action of the operator is determined solely by g . We test the operator against u . Using the summation by parts, we obtain the global dissipation relation:

$$\langle \mathcal{L}_h(f), u \rangle_{xv}^h = -\frac{\Delta x}{\Delta v} \sum_{p=1}^{N_x} \sum_{q=1}^{N_v-1} M_{p,q+1/2} (u_{p,q+1} - u_{p,q})^2.$$

We now seek a lower bound for the term on the right-hand side. Let $\mathcal{D}(u)$ be the spatial grid function representing the local dissipation:

$$[\mathcal{D}(u)]_p := \frac{1}{\Delta v^2} \sum_{q=1}^{N_v-1} (u_{p,q+1} - u_{p,q})^2.$$

Using the bound $M_{p,q+1/2} \geq M_{\min}$, we have the pointwise lower bound proportional to $\mathcal{D}(u)$. We apply the discrete Poincaré inequality on the uniform velocity grid. Let \bar{u} denote the spatial vector of arithmetic means (i.e., $[\bar{u}]_p = \frac{1}{N_v} \sum_q u_{p,q}$). Then pointwise:

$$\mathcal{D}(u) \geq \lambda_N \|u - \bar{u}\|_v^{h,2}.$$

To close the estimate, we need to relate the deviation from the arithmetic mean to the full norm. From the local mass conservation property, we have

$$\langle u, M \rangle_v^h = \langle g/M, M \rangle_v^h = \langle g, 1 \rangle_v^h = 0. \quad (5.8)$$

Using the decomposition $u = (u - \bar{u}) + \bar{u}$, the normalization $\langle 1, M \rangle_v^h = 1$ and (5.8), we obtain:

$$0 = \langle u - \bar{u}, M \rangle_v^h + \bar{u} \langle 1, M \rangle_v^h \implies \bar{u} = -\langle u - \bar{u}, M \rangle_v^h.$$

Applying the Cauchy–Schwarz inequality yields:

$$\bar{u}^2 = |\langle u - \bar{u}, M \rangle_v^h|^2 \leq \|u - \bar{u}\|_v^{h,2} \|M\|_v^{h,2} \leq L_v M_{\max} \|u - \bar{u}\|_v^{h,2}.$$

Substituting this back into the triangle inequality for $\|u\|_v^h$:

$$\|u\|_v^{h,2} \leq \left(\|u - \bar{u}\|_v^h + \|\bar{u}\|_v^h \right)^2 \leq \left(1 + \sqrt{L_v M_{\max}} \right)^2 \|u - \bar{u}\|_v^{h,2}.$$

Combining the local estimates and summing over all spatial nodes p yields:

$$-\langle \mathcal{L}_h(f), u \rangle_{xv}^h \geq M_{\min} \lambda_N \sum_{p=1}^{N_x} \|u - \bar{u}\|_v^{h,2} \Delta x \geq \frac{M_{\min} \lambda_N}{(1 + \sqrt{L_v M_{\max}})^2} \|u\|_{xv}^{h,2}.$$

This completes the proof. \square

Proposition 5.2 (Fluctuation-based projection bound). *Let P_X be the spatial projector onto the subspace $\text{span}\{X_i\}$. Let $\bar{\beta}$ denote the arithmetic mean of β_p over the spatial domain, and define the fluctuation $\delta\beta_p := \beta_p - \bar{\beta}$ and the inverse relative amplitude $C_\beta := \max_p (\beta_p \bar{\beta})^{-1}$. Then, for any distribution f in the range of P_X , the orthogonal projection of the Fokker–Planck operator is bounded by:*

$$\|(I - P_X)\mathcal{L}_h(f)\|_{xv}^h \leq \kappa_h \|f\|_{xv}^h, \quad (5.9)$$

where the fluctuation constant is defined by:

$$\kappa_h := \|\delta\beta\|_\infty \left(\frac{2\alpha_{\max}}{\Delta v^2} + C_\beta \frac{2}{\alpha_{\min} \Delta v^2} \right). \quad (5.10)$$

Proof. Recall that the separable stencil (3.6) defines the operator \mathcal{L}_h . We observe that this operator acts as a sum of tensor products involving multiplication by spatial weights β and β^{-1} :

$$\mathcal{L}_h = \beta \otimes \mathcal{T}^{(\alpha)} + \beta^{-1} \otimes \mathcal{T}^{(1/\alpha)}.$$

The velocity difference operators $\mathcal{T}^{(\alpha)}$ and $\mathcal{T}^{(1/\alpha)}$ act on a velocity grid function w as:

$$\begin{aligned} (\mathcal{T}^{(\alpha)} w)_q &= \frac{1}{\Delta v^2} (\alpha_{q+1/2} (w_{q+1} - w_q) - \alpha_{q-1/2} (w_q - w_{q-1})), \\ (\mathcal{T}^{(1/\alpha)} w)_q &= \frac{1}{\Delta v^2} (\alpha_{q+1/2}^{-1} (w_{q+1} - w_q) - \alpha_{q-1/2}^{-1} (w_q - w_{q-1})). \end{aligned}$$

Since the projector P_X acts only on the spatial coordinate, we can bound the two tensor terms separately.

Consider the first term involving β . We use the property that the scalar operator $\bar{\beta}I$ maps the subspace $\text{ran}(P_X)$ into itself. Thus, for any $f \in \text{ran}(P_X)$, the orthogonal complement vanishes: $(I - P_X)(\bar{\beta}f) = 0$. We write:

$$(I - P_X)(\beta f) = (I - P_X)(\beta f - \bar{\beta}f) = (I - P_X)((\beta - \bar{\beta})f).$$

Since $\|I - P_X\|_x^h \leq 1$, we bound the norm of the above:

$$\|(I - P_X)(\beta f)\|_{xv}^h \leq \|(\beta - \bar{\beta})f\|_{xv}^h \leq \max_p |\beta_p - \bar{\beta}| \|f\|_{xv}^h = \|\delta\beta\|_\infty \|f\|_{xv}^h.$$

For the second term involving β^{-1} , we similarly choose the scalar constant $\bar{\beta}^{-1}$. The spatial coefficient variation is bounded algebraically:

$$|\beta_p^{-1} - \bar{\beta}^{-1}| = \left| \frac{\bar{\beta} - \beta_p}{\beta_p \bar{\beta}} \right| = \frac{1}{\beta_p \bar{\beta}} |\beta_p - \bar{\beta}| \leq C_\beta \|\delta\beta\|_\infty.$$

Thus, the second spatial term satisfies $\|(I - P_X)(\beta^{-1}f)\|_{xv}^h \leq C_\beta \|\delta\beta\|_\infty \|f\|_{xv}^h$.

Finally, we bound the velocity operators. By applying the triangle inequality to the difference stencils defined above, we observe that each operator acts on neighboring grid points with weights bounded by α_{\max} (or α_{\min}^{-1}). A direct estimation of the induced norms yields:

$$\|\mathcal{T}^{(\alpha)}\|_v^h \leq \frac{2\alpha_{\max}}{\Delta v^2} \quad \text{and} \quad \|\mathcal{T}^{(1/\alpha)}\|_v^h \leq \frac{2}{\alpha_{\min} \Delta v^2}.$$

Combining these estimates with the spatial bounds yields the total constant κ_h defined in (5.10). \square

5.3 Main results

We now prove the AP property. We assume the formal asymptotic regime $0 < \varepsilon \ll \Delta t \ll 1$, wherein the numerical solution f and its discrete derivatives are treated as bounded (smooth) $\mathcal{O}(1)$ quantities. Additionally, we require that the field fluctuation is small relative to the dissipation gap:

Assumption 5.1 (Small-fluctuation regime). *We assume that the field fluctuation κ_h (defined in Proposition 5.2) satisfies*

$$\kappa_h M_{\max}^{n+1} < \gamma_h, \quad (5.11)$$

where γ_h is the coercivity constant from Proposition 5.1 and $M_{\max}^{n+1} = \max_{p,q} M_{p,q+1/2}^{n+1}$.

Theorem 5.3 (AP property up to spatial fluctuation). *Let f^{n+1} be the low-rank solution obtained after the L -step update. Let $\rho^{n+1} = \langle f^{n+1}, 1 \rangle_v^h$ be the macroscopic density vector. Let G^{n+1} denote the discrete residual defined by the time difference and advection operators (see (5.14)). Under Assumption 5.1 and the formal asymptotic regime assumptions (implying $\|G^{n+1}\|_{xv}^h = \mathcal{O}(1)$), let $\Theta := \gamma_h / (\gamma_h - \kappa_h M_{\max}^{n+1}) \geq 1$. Then, the Fokker–Planck residual satisfies*

$$\|\mathcal{L}_h^{n+1}(f^{n+1})\|_{xv}^h \leq \Theta \left(\varepsilon \|G^{n+1}\|_{xv}^h + \kappa_h M_{\max}^{n+1} \sqrt{L_v} \|\rho^{n+1}\|_x^h \right), \quad (5.12)$$

and

$$\|f^{n+1} - \rho^{n+1} M^{n+1}\|_{xv}^h \leq \frac{M_{\max}^{n+1}}{\gamma_h} \Theta \left(\varepsilon \|G^{n+1}\|_{xv}^h + \kappa_h M_{\max}^{n+1} \sqrt{L_v} \|\rho^{n+1}\|_x^h \right). \quad (5.13)$$

Proof. We focus our analysis on the L-step because it determines the final state f^{n+1} . Recall the L-step update (4.6) projected onto the updated spatial basis X_i^{n+1} :

$$\frac{L_i^{n+1} - L_i^{(2)}}{\Delta t} = -\langle \mathcal{A}_h(f^{(2)}), X_i^{n+1} \rangle_x^h + \frac{1}{\varepsilon} \langle \mathcal{L}_h^{n+1}(f^{n+1}), X_i^{n+1} \rangle_x^h.$$

Multiplying by X_i^{n+1} and summing over i , we reconstruct the full distribution update projected onto the spatial subspace. Let P_X^{n+1} be the orthogonal projector onto $\text{span}\{X_i^{n+1}\}$. Rearranging the update equation to isolate the Fokker–Planck term yields:

$$P_X^{n+1} \mathcal{L}_h^{n+1}(f^{n+1}) = \varepsilon \underbrace{\left[\frac{f^{n+1} - f^{(2)}}{\Delta t} + P_X^{n+1} \mathcal{A}_h(f^{(2)}) \right]}_{:= G^{n+1}}. \quad (5.14)$$

In the assumed asymptotic regime, the term G^{n+1} depends only on bounded transport and time-difference operators acting on the smooth solution; thus $\|G^{n+1}\|_{xv}^h = \mathcal{O}(1)$ as $\varepsilon \rightarrow 0$.

We now decompose the Fokker–Planck operator image into projected and orthogonal components:

$$\|\mathcal{L}_h^{n+1}(f^{n+1})\|_{xv}^h \leq \|P_X^{n+1} \mathcal{L}_h^{n+1}(f^{n+1})\|_{xv}^h + \|(I - P_X^{n+1}) \mathcal{L}_h^{n+1}(f^{n+1})\|_{xv}^h.$$

From (5.14), the projected component is exactly $\varepsilon \|G^{n+1}\|_{xv}^h$. For the orthogonal component, since f^{n+1} lies in the range of P_X^{n+1} , Proposition 5.2 bounds the orthogonal component by $\kappa_h \|f^{n+1}\|_{xv}^h$.

To utilize the coercivity estimate, we use the micro–macro decomposition $f^{n+1} = \rho^{n+1} M^{n+1} + g^{n+1}$. We bound the state norm by

$$\|f^{n+1}\|_{xv}^h \leq \|\rho^{n+1} M^{n+1}\|_{xv}^h + \|g^{n+1}\|_{xv}^h \leq M_{\max}^{n+1} \sqrt{L_v} \|\rho^{n+1}\|_x^h + \|g^{n+1}\|_{xv}^h.$$

We now test the operator against the relative fluctuation g^{n+1}/M^{n+1} . Proposition 5.1 provides the lower bound $-\langle \mathcal{L}_h^{n+1}(f^{n+1}), g^{n+1}/M^{n+1} \rangle_{xv}^h \geq \gamma_h \|g^{n+1}/M^{n+1}\|_{xv}^{h,2}$. Conversely, decomposing \mathcal{L}_h^{n+1} into $\varepsilon G^{n+1} + (I - P_X^{n+1}) \mathcal{L}_h^{n+1}$ and testing against g^{n+1}/M^{n+1} yields an upper bound:

$$\begin{aligned} -\langle \mathcal{L}_h^{n+1}(f^{n+1}), g^{n+1}/M^{n+1} \rangle_{xv}^h &\leq (\varepsilon \|G^{n+1}\|_{xv}^h + \kappa_h \|f^{n+1}\|_{xv}^h) \|g^{n+1}/M^{n+1}\|_{xv}^h \\ &\leq \left(\varepsilon \|G^{n+1}\|_{xv}^h + \kappa_h [M_{\max}^{n+1} \sqrt{L_v} \|\rho^{n+1}\|_x^h + \|g^{n+1}\|_{xv}^h] \right) \|g^{n+1}/M^{n+1}\|_{xv}^h. \end{aligned}$$

Using the inequality $\|g^{n+1}\|_{xv}^h = \|M^{n+1}(g^{n+1}/M^{n+1})\|_{xv}^h \leq M_{\max}^{n+1} \|g^{n+1}/M^{n+1}\|_{xv}^h$, we can absorb the $\|g^{n+1}\|$ term. Assuming $\|g^{n+1}/M^{n+1}\|_{xv}^h > 0$, we divide by $\|g^{n+1}/M^{n+1}\|_{xv}^h$ and rearrange terms:

$$(\gamma_h - \kappa_h M_{\max}^{n+1}) \|g^{n+1}/M^{n+1}\|_{xv}^h \leq \varepsilon \|G^{n+1}\|_{xv}^h + \kappa_h M_{\max}^{n+1} \sqrt{L_v} \|\rho^{n+1}\|_x^h.$$

Identifying the amplification factor $\Theta = \gamma_h / (\gamma_h - \kappa_h M_{\max}^{n+1})$, we obtain the bound for $\|g^{n+1}/M^{n+1}\|_{xv}^h$. The distance to equilibrium is simply $\|f^{n+1} - \rho^{n+1} M^{n+1}\|_{xv}^h = \|g^{n+1}\|_{xv}^h \leq M_{\max}^{n+1} \|g^{n+1}/M^{n+1}\|_{xv}^h$, which yields (5.13). The residual bound (5.12) follows by substituting this back into the norm decomposition of \mathcal{L}_h . \square

Remark 5.4. *If the electric field is spatially constant (even if large), we may choose $\bar{\beta} = \beta_p$, implying $\delta\beta \equiv 0$ and $\kappa_h = 0$. In this case, the error is purely $\mathcal{O}(\varepsilon)$, recovering the strong AP property.*

Remark 5.5. *The analysis in this section assumes the electric field E^{n+1} is given and fixed during the kinetic update. In the full VPFP system, E is coupled to ρ via the Poisson equation. A complete AP analysis of the fully nonlinear coupled system would require accounting for errors in the macroscopic field solver, which is beyond the scope of this work.*

Remark 5.6. *Although Theorem 5.3 only proves AP property up to the spatial fluctuation $\mathcal{O}(\kappa_h)$, we observe in the numerical experiments that the first-order scheme exhibits an AP error of $\mathcal{O}(\varepsilon)$, regardless of the field fluctuation.*

6 Numerical experiments

We validate the accuracy, efficiency, and AP property of the proposed first-order and second-order low-rank IMEX schemes. All numerical tests are performed in a 1D1V phase space with periodic boundary condition in x and zero flux boundary condition in the truncated velocity domain $[-6, 6]$.

6.1 Convergence and AP tests

We consider two types of initial data:

Non-equilibrium initial data (used for the first-order scheme). We take a shifted Gaussian in v with a spatially varying density,

$$f_{\text{neq}}^0(x, v) = \frac{\rho^0(x)}{\sqrt{2\pi}} \exp\left(-\frac{(v - 1.5)^2}{2}\right), \quad \rho^0(x) = \sqrt{2\pi} (2 + \cos(2\pi x)), \quad x \in [0, 1],$$

and the background charge

$$\eta(x) = \frac{2\sqrt{2\pi}}{I_0(1)} e^{\cos(2\pi x)},$$

so that the neutrality condition $\int_0^1 (\rho^0 - \eta) dx = 0$ holds. Here I_0 denotes the modified Bessel function of the first kind of order zero, and $I_0(1) \approx 1.2661$. The initial electric field E^0 is obtained from the Poisson equation

$$-\partial_{xx}\phi^0 = \rho^0(x) - \eta(x), \quad E^0(x) = -\partial_x\phi^0.$$

Equilibrium initial data (used for the second-order scheme). For the second-order scheme, the AP property in the full-tensor framework is guaranteed when the initial data is close to the equilibrium. Accordingly, for the second-order low-rank scheme, we consider equilibrium initial data of the form

$$f_{\text{eq}}^0(x, v) = \frac{\rho^0(x)}{\sqrt{2\pi}} \exp\left(-\frac{(v - E^0(x))^2}{2}\right),$$

where $\rho^0(x)$ and $E^0(x)$ are the same as above.

Let $\|\cdot\|_{L_{x,v}^1}$ denote the discrete L^1 norm in phase space induced by the (x, v) grid and $\|\cdot\|_{L_v^1}$ the corresponding L^1 norm in v at fixed x . To measure the convergence rate in time, we consider a sequence of time steps

$$\Delta t_0 > \Delta t_1 > \dots > \Delta t_K, \quad \Delta t_{k+1} = \frac{\Delta t_k}{2},$$

and for each k we evolve the scheme up to a fixed final time T with time step Δt_k . The time-discretization error at level k is defined by the difference between two successive time steps,

$$\mathcal{E}_{\Delta t_k}(T) := \|f^{\Delta t_k}(T) - f^{\Delta t_{k+1}}(T)\|_{L_{x,v}^1}. \quad (6.1)$$

If the scheme is p th-order accurate in time, then for small Δt_k one expects $\mathcal{E}_{\Delta t_k}(T) \approx C (\Delta t_k)^p$, so the slope of $\mathcal{E}_{\Delta t_k}(T)$ versus Δt_k on a log-log plot reflects the observed convergence rate p .

To assess AP property, we quantify the deviation of f from its local Maxwellian $\rho(x, t)M(x, v, t)$ and monitor the global discrete $L^1_{x,v}$ error

$$\mathcal{E}_{AP}(t) := \|f(\cdot, \cdot, t) - \rho(\cdot, t)M(\cdot, \cdot, t)\|_{L^1_{x,v}}. \quad (6.2)$$

First-order scheme. For the first-order low-rank IMEX scheme, we use $(N_x, N_v) = (64, 64)$ and rank $r = 10$. We consider both the kinetic regime $\varepsilon = 1$ and the high-field regime $\varepsilon = 10^{-6}$. For the time-step convergence study we take

$$\Delta t_0 = 10^{-3}, \quad \Delta t_{k+1} = \frac{\Delta t_k}{2}, \quad k = 0, \dots, 4, \quad T_{\max} = 5 \times 10^{-3}.$$

Figure 1(a) shows $\mathcal{E}_{\Delta t_k}(T_{\max})$ versus Δt_k on a log-log scale. The observed slopes are close to one for both $\varepsilon = 1$ and $\varepsilon = 10^{-6}$, indicating first-order convergence in time that is essentially uniform with respect to ε .

For the AP test we fix $\Delta t = 2.5 \times 10^{-3}$, $T_{\max} = 0.1$, and $r = 10$, and monitor the global AP error $\mathcal{E}_{AP}(t)$ defined in (6.2). As shown in Figure 1(b), the error decays rapidly over a few time steps and then saturates at a level proportional to ε . This behavior is consistent with the AP property of the first-order full-tensor scheme, indicating that the low-rank formulation retains robustness to non-equilibrium initial data.

Second-order scheme. For the second-order low-rank IMEX scheme, we again use $(N_x, N_v) = (64, 64)$. When $\varepsilon = O(1)$, there is no guarantee that the solution is close to an equilibrium manifold. To separate time-discretization error from rank-truncation error in the convergence study, we therefore use a slightly larger rank $r = 15$ for $\varepsilon = 1$. When ε is very small, the solution is expected to remain close to a local Maxwellian; in this case we choose a smaller rank $r = 6$ for $\varepsilon = 10^{-6}$ to illustrate the efficiency of the low-rank approach in the fluid regime. The time-step convergence study uses

$$\Delta t_0 = 5 \times 10^{-5}, \quad \Delta t_{k+1} = \frac{\Delta t_k}{2}, \quad k = 0, \dots, 4, \quad T_{\max} = 5 \times 10^{-4}.$$

Figure 1(c) reports $\mathcal{E}_{\Delta t_k}(T_{\max})$ versus Δt_k . The measured slopes are close to two for both values of ε , confirming second-order convergence in time and suggesting that the order is essentially uniform in the kinetic and fluid regimes.

For the AP test we fix $\Delta t = 5 \times 10^{-5}$ and $T_{\max} = 2 \times 10^{-3}$, and monitor $\mathcal{E}_{AP}(t)$. The results in Figure 1(d) demonstrate rapid relaxation towards the local Maxwellian with a plateau at a level proportional to ε , consistent with the AP theory for the second-order full-tensor scheme.

6.2 Mixed regime

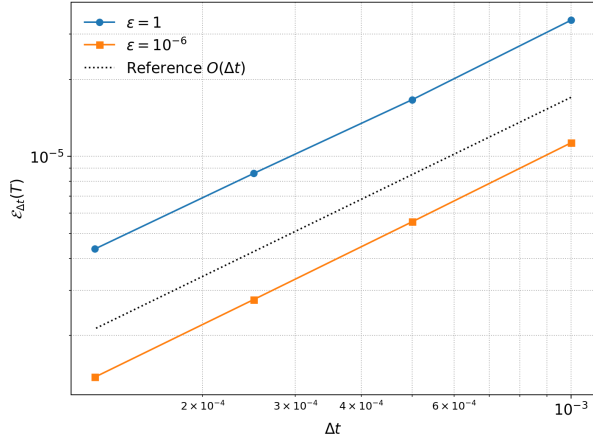
In the rest of the tests, we use the first-order low-rank IMEX scheme.

We prescribe a spatially varying Knudsen number

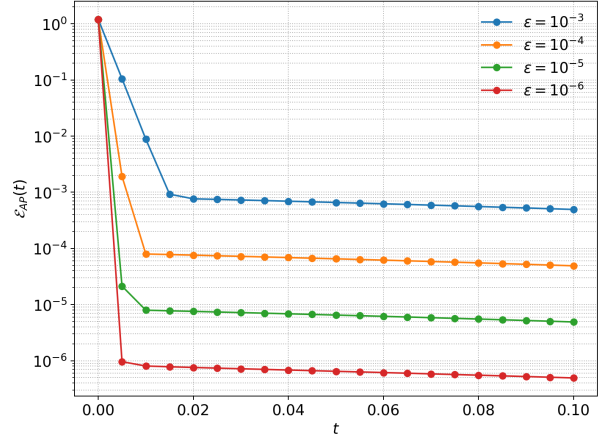
$$\varepsilon(x) = \begin{cases} \varepsilon_0 + \frac{1}{2}(\tanh(5 - 10x) + \tanh(5 + 10x)), & x \leq 0.3, \\ \varepsilon_0, & x > 0.3, \end{cases} \quad \varepsilon_0 = 10^{-3}, \quad x \in [-1, 1],$$

so that the left part of the domain has $\varepsilon(x)$ of order one, while the right part has a smaller, nearly constant value $\varepsilon(x) \approx \varepsilon_0$. The initial density and distribution are

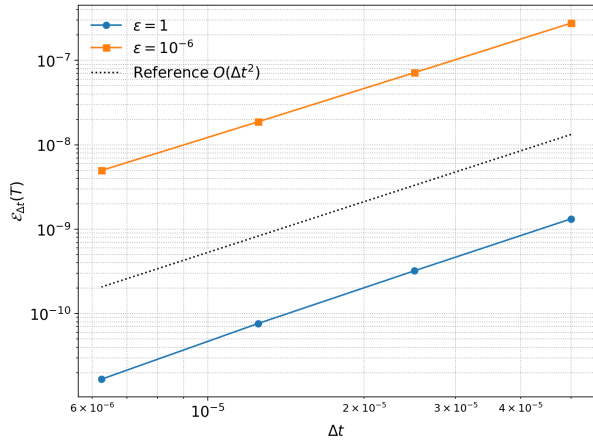
$$\rho^0(x) = \frac{\sqrt{2\pi}}{6}(2 + \sin(\pi x)), \quad f^0(x, v) = \frac{\rho^0(x)}{\sqrt{2\pi}} \exp\left(-\frac{(v - E^0(x))^2}{2}\right),$$



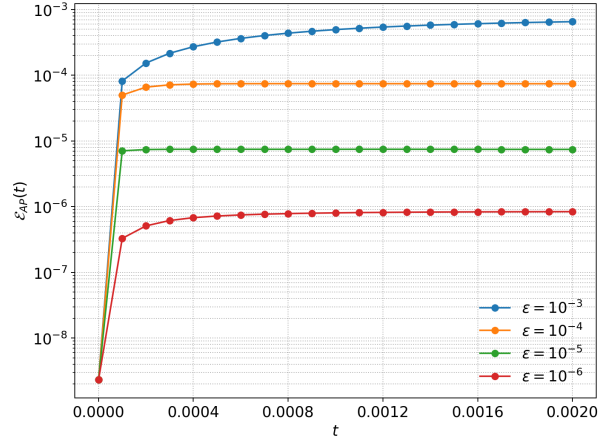
(a) First-order: convergence of f vs. Δt for $\varepsilon = 1$ and $\varepsilon = 10^{-6}$.



(b) First-order: global AP error $\mathcal{E}_{AP}(t)$ over time.



(c) Second-order: convergence of f vs. Δt for $\varepsilon = 1$ and $\varepsilon = 10^{-6}$.



(d) Second-order: global AP error $\mathcal{E}_{AP}(t)$ over time.

Figure 1: Time-step convergence and AP property for the first-order (top) and second-order (bottom) low-rank IMEX schemes.

with background charge

$$\eta(x) = C_\eta e^{\cos(\pi x)},$$

where the constant C_η is chosen so that the neutrality condition

$$\int_{-1}^1 (\eta(x) - \rho^0(x)) dx = 0$$

holds (numerically, $C_\eta \approx 0.6599$). Thus f^0 is a local Maxwellian with density $\rho^0(x)$ and field $E^0(x)$. We use $N_x = 100$, $N_v = 128$, a time step $\Delta t = 10^{-4}$, and a moderate fixed rank $r = 13$ for the low-rank approximation.

Figure 2 illustrates the density and electric field at $t = 0.10$ and $t = 0.30$, demonstrating that the low-rank scheme accurately reproduces the macroscopic evolution in both regions. Figure 3 compares the phase portraits of the full-tensor reference solution and the low-rank solution, alongside their absolute difference at the final time. The low-rank scheme exhibits excellent agreement with the full-tensor benchmark. These results confirm that a moderate rank is sufficient to effectively capture the dominant phase-space structures in both the order-one and small- $\varepsilon(x)$ subdomains.

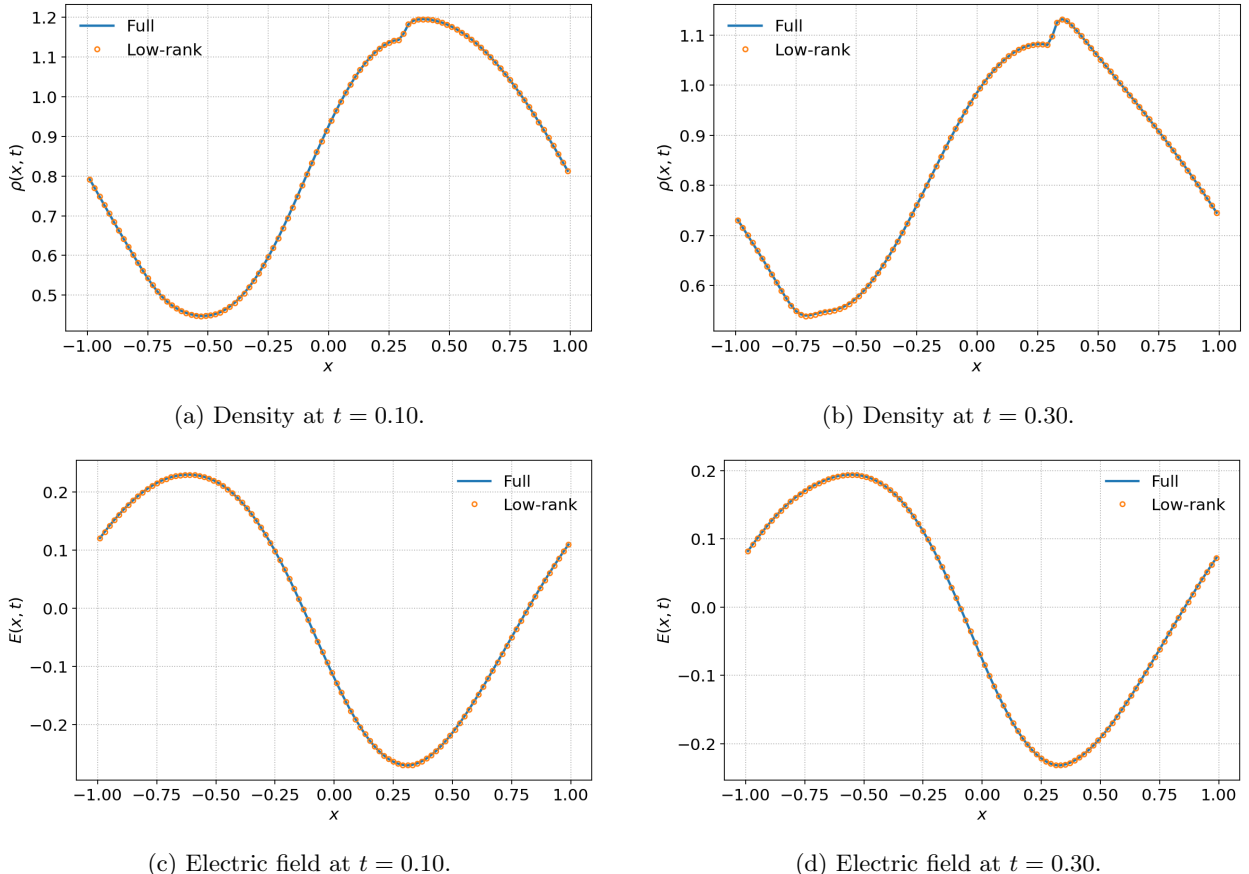


Figure 2: Mixed-regime test: comparison of macroscopic density (top row) and electric field (bottom row) between the full-tensor reference solution (solid lines) and the first-order low-rank IMEX scheme (circles) at $t = 0.10$ and $t = 0.30$.

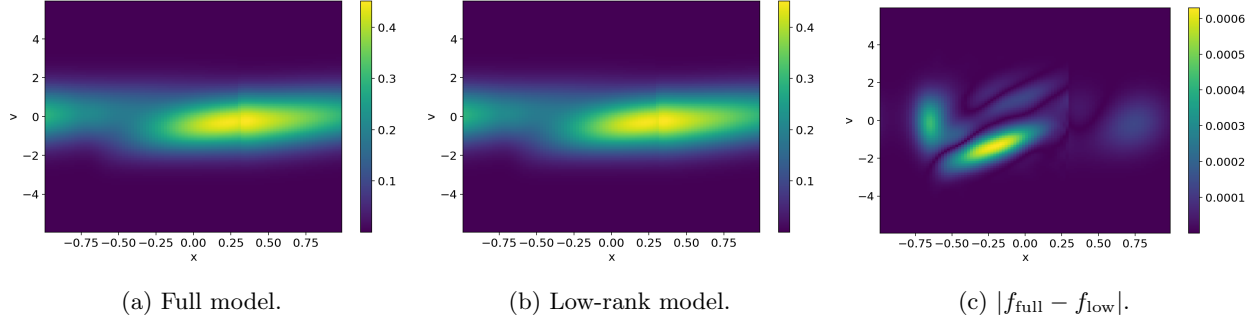


Figure 3: Phase plots in the mixed regime test: full tensor, low-rank, and absolute difference.

Finally, Figure 4 reports the spatial profile of $\varepsilon(x)$ together with the pointwise AP error

$$\mathcal{E}_{AP}(x, t) = \|f(x, \cdot, t) - \rho(x, t)M(x, \cdot, t)\|_{L_v^1}$$

at $t = 0.10$ and $t = 0.30$. The error is of order $\mathcal{O}(\varepsilon(x))$, consistent with the expected AP behavior and with the mixed-regime results for the full-tensor reference scheme.

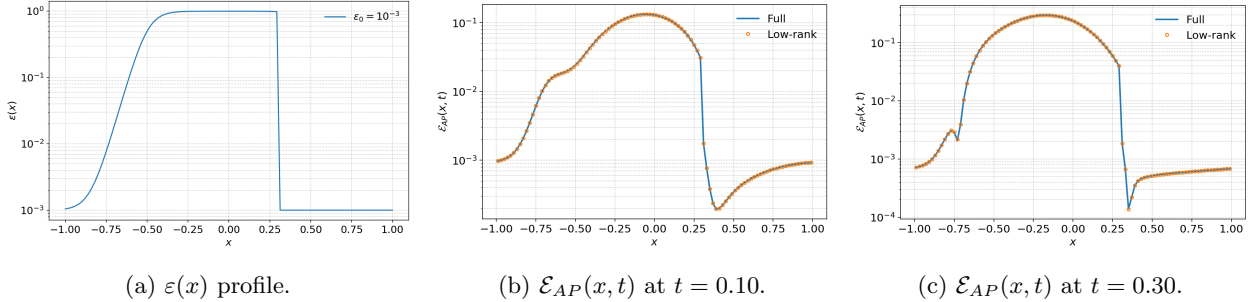


Figure 4: Spatial profiles for the mixed-regime test: (a) the Knudsen number $\varepsilon(x)$; (b) and (c) the pointwise AP error $\mathcal{E}_{AP}(x, t)$ at $t = 0.10$ and $t = 0.30$, respectively.

6.3 Bump-on-tail instability

The bump-on-tail instability (adapted from [4]) serves as a nonlinear kinetic benchmark. The initial distribution consists of a thermal background and a cold shifted beam:

$$f^0(x, v) = \frac{\rho^0(x)}{\sqrt{2\pi}} \left(e^{-\frac{v^2}{2}} + e^{-\frac{(v-1.5)^2}{2T_{\text{cold}}}} \right), \quad T_{\text{cold}} = 5 \times 10^{-3},$$

with spatially localized density and background charge

$$\rho^0(x) = 0.3 + \exp\left(-\frac{(x-0.3)^2}{0.01}\right), \quad \eta(x) = 0.3 + \exp\left(-\frac{(x-0.6)^2}{0.01}\right),$$

The Knudsen number is uniform: $\varepsilon(x) \equiv \varepsilon_0$. We take $N_x = 100$, $N_v = 128$, time step $\Delta t = 10^{-3}$, and rank $r = 6$. We examine two regimes:

- **Fluid regime:** $\varepsilon_0 = 10^{-6}$, final time $T = 0.5$.
- **Kinetic regime:** $\varepsilon_0 = 1$, final time $T = 0.1$.

The rank $r = 6$ is deliberately small relative to (N_x, N_v) in order to demonstrate that the first-order low-rank IMEX scheme can capture the main bump-on-tail dynamics with only a few modes. We note that Coughlin and Hu [4] simulated this same benchmark using a quotient-based DLR method for f/M ; while their approach is optimally efficient ($r \approx 3, 4$) in the fluid limit, it requires significantly higher ranks ($r \approx 20$) to capture the non-equilibrium dynamics in the kinetic regime. In contrast, our proposed method maintains high accuracy with a consistently small rank ($r = 6$) across both regimes.

Figure 5 displays the macroscopic density and electric field. The first-order low-rank IMEX scheme yields stable results that are consistent with the full-tensor reference solutions in both kinetic and fluid regimes. This confirms that the method effectively captures the correct macroscopic dynamics in these scenarios.

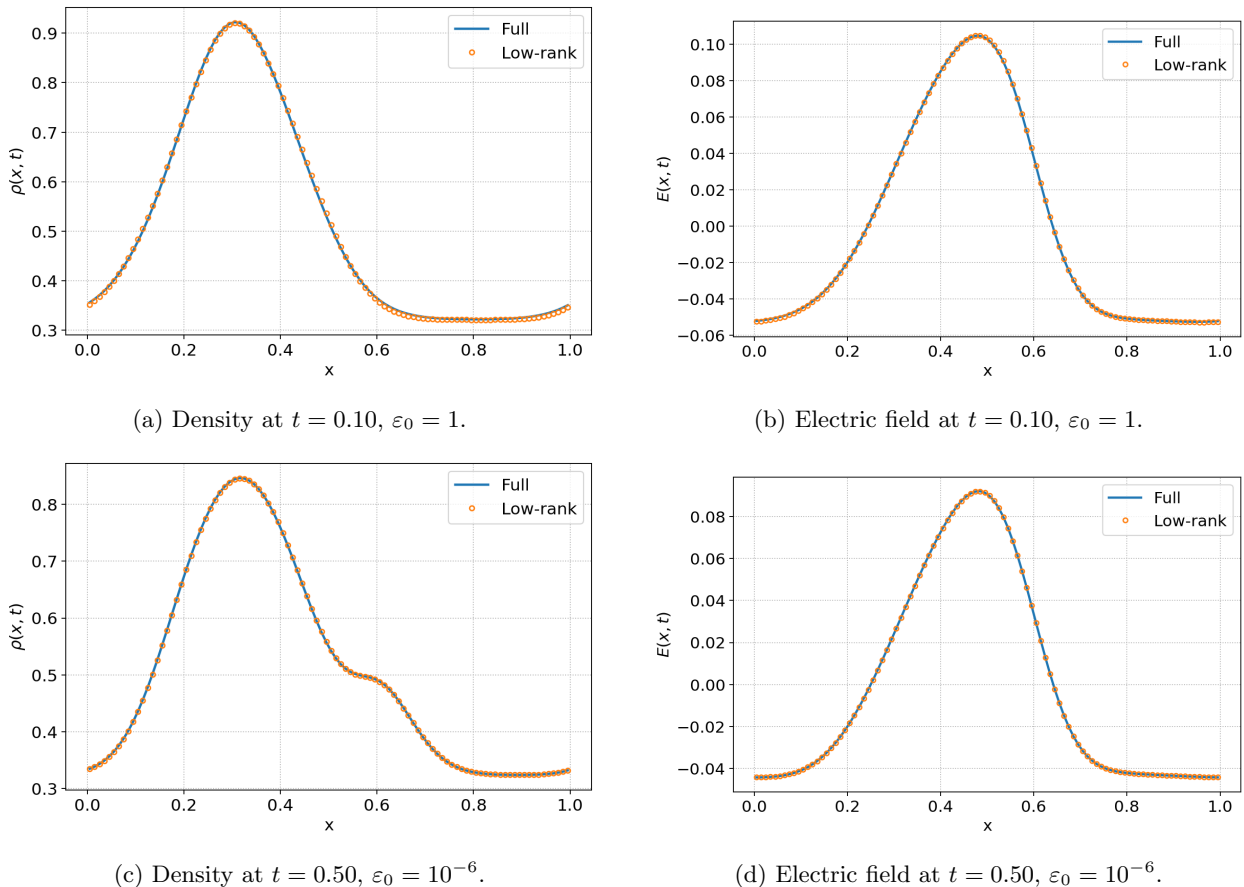


Figure 5: Bump-on-tail test: macroscopic density and electric field in the kinetic ($t = 0.10, \varepsilon_0 = 1$) and fluid ($t = 0.50, \varepsilon_0 = 10^{-6}$) regimes.

To visualize the phase-space dynamics, Figures 6 and 7 show phase space plots of the full-tensor reference solution, the low-rank solution, and their absolute difference at representative times in the kinetic and fluid regimes, respectively. In the kinetic case ($t = 0.10, \varepsilon_0 = 1$), the low-rank solution approximates the full-tensor reference solution well, accurately capturing the phase-space structures. In the fluid case

($t = 0.50$, $\varepsilon_0 = 10^{-6}$), the phase-space distribution has nearly relaxed to a local Maxwellian, and the low-rank approximation is extremely accurate across the domain.

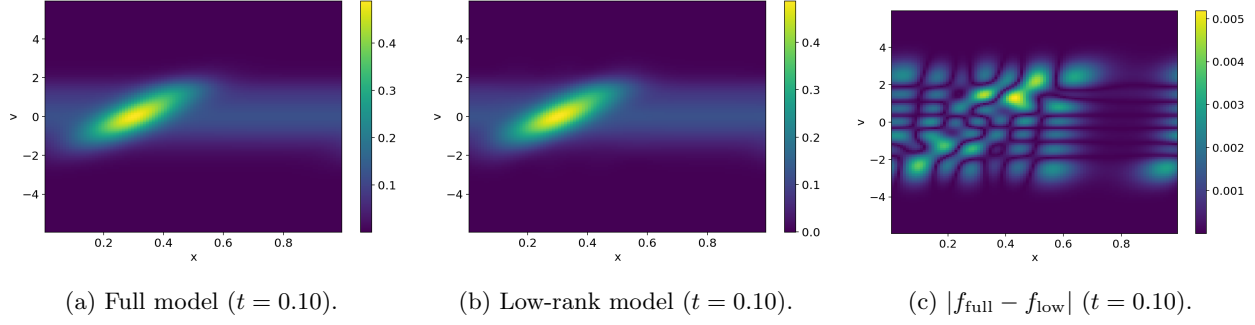


Figure 6: Bump-on-tail phase space plots at $t = 0.10$ in the kinetic regime ($\varepsilon_0 = 1$).

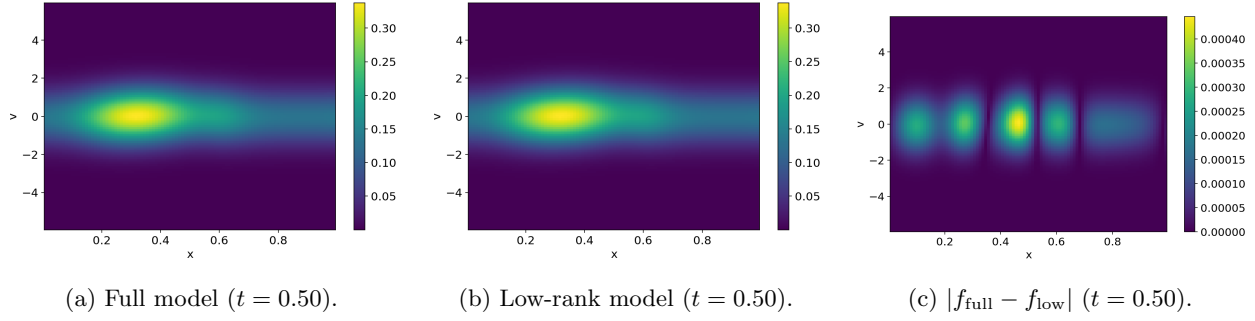
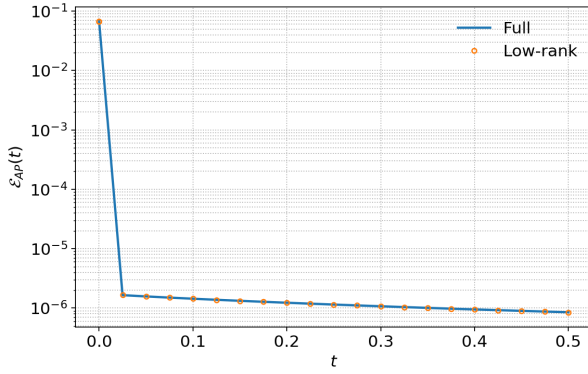


Figure 7: Bump-on-tail phase space plots at $t = 0.50$ in the fluid regime ($\varepsilon_0 = 10^{-6}$).

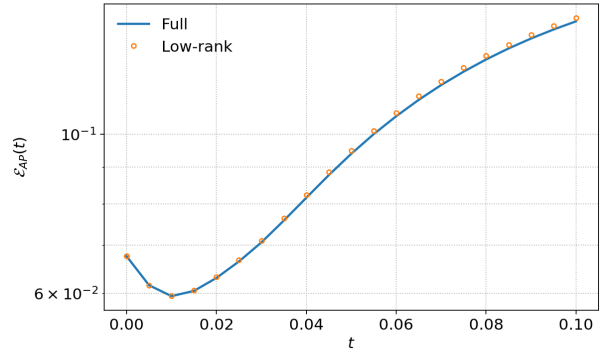
Finally, Figure 8 plots the global AP error $\mathcal{E}_{AP}(t)$ for both regimes. In the fluid case ($\varepsilon_0 = 10^{-6}$) the error decays rapidly and remains very small, indicating fast relaxation to the local Maxwellian shape. In the kinetic case ($\varepsilon_0 = 1$) the deviation remains larger but bounded, reflecting the persistent kinetic structures associated with the bump-on-tail instability.

7 Conclusions

We have presented a dynamical low-rank (DLR) method for the Vlasov–Poisson–Fokker–Planck system that effectively addresses both the curse of dimensionality and the stiffness of the high-field regime. The cornerstone of this method is a conservative, separable discretization of the Fokker–Planck operator. By constructing a three-point stencil where coefficients factor into space–only and velocity–only components, we enable the efficient implicit treatment of the Fokker–Planck operator directly on the low-rank manifold without requiring expensive full-tensor reconstruction. To handle the stiffness within the low-rank framework, we proposed both first-order and second-order schemes using proper IMEX treatment to ensure stability. We provided a theoretical analysis for the first-order low-rank scheme, proving an asymptotic–preserving property in the case of small spatial field fluctuations. Numerical benchmarks demonstrate that the proposed methods are asymptotically preserving and robust, maintaining the reduced computational and storage cost while accurately capturing macroscopic limits and kinetic structures at modest ranks.



(a) $\mathcal{E}_{AP}(t)$ vs. t (fluid, $\varepsilon_0 = 10^{-6}$).



(b) $\mathcal{E}_{AP}(t)$ vs. t (kinetic, $\varepsilon_0 = 1$).

Figure 8: Bump-on-tail AP error $\mathcal{E}_{AP}(t)$ over time for the first-order low-rank scheme in fluid and kinetic regimes.

Acknowledgement

This work was partially supported by DOE grant DE-SC0023164, NSF grants DMS-2409858 and IIS-2433957, and DoD MURI grant FA9550-24-1-0254.

References

- [1] B. CARREL, D. KRESSNER, H. Y. LAM, AND B. VANDEREYCKEN, *Interpolatory dynamical low-rank approximation: Theoretical foundations and algorithms*, arXiv preprint arXiv:2510.19518, (2025).
- [2] J. A. CARRILLO, K. CRAIG, L. WANG, AND C. WEI, *Variational asymptotic preserving scheme for the Vlasov–Poisson–Fokker–Planck system*, Multiscale Modeling & Simulation, 19 (2021), pp. 378–417.
- [3] C. CERCIGNANI, I. M. GAMBA, J. W. JEROME, AND C.-W. SHU, *Device benchmark comparisons via kinetic, hydrodynamic, and high-field models*, Computer Methods in Applied Mechanics and Engineering, 181 (2000), pp. 381–392.
- [4] J. COUGHLIN AND J. HU, *Efficient dynamical low-rank approximation for the Vlasov-Ampère-Fokker-Planck system*, Journal of Computational Physics, 470 (2022), p. 111590.
- [5] A. DEKTOR AND L. EINKEMMER, *Interpolatory dynamical low-rank approximation for the 3+ 3d Boltzmann–BGK equation*, Journal of Computational Physics, (2025), p. 114515.
- [6] J. DOUGHERTY, *Model Fokker-Planck equation for a plasma and its solution*, The Physics of Fluids, 7 (1964), pp. 1788–1799.
- [7] L. EINKEMMER, K. KORMANN, J. KUSCH, R. MCCLARREN, AND J.-M. QIU, *A review of low-rank methods for time-dependent kinetic simulations*, J. Comput. Phys., 538 (2025), p. 114191.
- [8] F. FILBET AND S. JIN, *A class of asymptotic-preserving schemes for kinetic equations and related problems with stiff sources*, Journal of Computational Physics, 229 (2010), pp. 7625–7648.

- [9] S. JIN, *Efficient asymptotic-preserving (AP) schemes for some multiscale kinetic equations*, SIAM Journal on Scientific Computing, 21 (1999), pp. 441–454.
- [10] S. JIN, *Asymptotic-preserving schemes for multiscale physical problems*, Acta Numerica, 31 (2022), pp. 1–82.
- [11] S. JIN AND L. WANG, *An asymptotic preserving scheme for the Vlasov-Poisson-Fokker-Planck system in the high field regime*, Acta Mathematica Scientia, 31 (2011), pp. 2219–2232.
- [12] S. JIN AND B. YAN, *A class of asymptotic-preserving schemes for the Fokker-Planck-Landau equation*, J. Comput. Phys., 230 (2011), pp. 6420–6437.
- [13] O. KOCH AND C. LUBICH, *Dynamical low-rank approximation*, SIAM Journal on Matrix Analysis and Applications, 29 (2007), pp. 434–454.
- [14] C. LUBICH, *From quantum to classical molecular dynamics: reduced models and numerical analysis*, European Mathematical Society, Zürich, 2008.
- [15] C. LUBICH AND I. V. OSELEDETS, *A projector-splitting integrator for dynamical low-rank approximation*, BIT Numerical Mathematics, 54 (2014), pp. 171–188.
- [16] J. NIETO, F. POUPAUD, AND J. SOLER, *High-field limit for the vlasov-poisson-fokker-planck system*, Archive for rational mechanics and analysis, 158 (2001), pp. 29–59.
- [17] F. POUPAUD, *Runaway phenomena and fluid approximation under high fields in semiconductor kinetic theory*, ZAMM-Journal of Applied Mathematics and Mechanics/Zeitschrift für Angewandte Mathematik und Mechanik, 72 (1992), pp. 359–372.
- [18] F. POUPAUD AND J. SOLER, *Parabolic limit and stability of the Vlasov-Fokker-Planck system*, Mathematical Models and Methods in Applied Sciences, 10 (2000), pp. 1027–1045.
- [19] C. VILLANI, *A review of mathematical topics in collisional kinetic theory*, in Handbook of mathematical fluid dynamics, Vol. I, North-Holland, 2002, pp. 71–305.
- [20] S. ZHANG AND J. HU, *On the stability of the low-rank projector-splitting integrator for hyperbolic and parabolic equations*, arXiv preprint arXiv:2507.15192, (2025).
- [21] Y. ZHU AND S. JIN, *Hypocoercivity and uniform regularity for the Vlasov-Poisson-Fokker-Planck system with uncertainty and multiple scales*, SIAM Journal on Mathematical Analysis, 49 (2017), pp. 1794–1826.